# Crystal Structure Evolution of BaBrCl and BaBrCl:5%Eu up to 800°C by Neutron Diffraction

D. R. Onken,[a] R. T. Williams,[a] D. Perrodin,,[b] T. Shalapska,[b] E. D. Bourret,[b] A. S. Tremsin,[c] and Sven C. Vogel[d]

BaBrCl:Eu is a promising scintillator material; however, the crystal growth yield must be improved for it to become commercially viable. This study measures strain accumulations in the crystal lattice which can contribute to cracking during post-growth cooling. Neutron diffraction is used to measure the crystal structure of undoped and 5 mol% europium-doped BaBrCl from 30°C up to 800°C, approaching the melting point. Rietveld analysis of this data obtains the temperature dependence of the thermal and chemical strain in BaBrCl. In particular, anisotropic thermal expansion is measured, with expansion along the b-axis nearly double the expansion along the a- and c-axes. Additionally, the chemical strain from the incorporation of europium atoms peaks around 400°C, explaining cracking frequently observed in that temperature range.

## 1 Introduction

BaBrCl is a recently developed scintillator material which has the potential to bridge the gap between high-resolution yet high-cost scintillators such as $LaBr_3$ and relatively low-resolution yet low-cost scintillators such as CsI or NaI. Doped with 5 mol% europium, BaBrCl has a light yield of 52,000 photons/MeV and an energy resolution of 3.55% at 662 keV[1]. Additionally, it is less hygroscopic than $LaBr_3$ and may have more potential for broad implementation[2]. However, to become an economically viable commercial scintillator, the crystal growth yield must be improved. As with many inorganic scintillator crystals, cracking poses a challenge during crystal growth of BaBrCl, particularly when adding the Eu dopant. In its implementation as a radiation detector, the BaBrCl host absorbs ionizing radiation and the Eu ion is the recombination center that has been found to be best suited to convert that energy into countable photons. The wavelength of Eu luminescence around 410 nm is well-matched to the wavelength sensitivity of photomultiplier tubes, which are coupled with the scintillator crystal in the radiation detector. Eu has the same valence state and a similar atomic radius as the Ba it substitutes, so it is more likely to be incorporated into the BaBrCl crystal with greater uniformly and with less strain. However, this strain from Eu doping is still significant, and can contribute to crystal cracking. Yan et al. acknowledged the issue of cracking during post-growth cooling in Czochralski growth of 5% Eu-doped BaBrCl, noting the need for additional insulation and reflectors to make a more isothermal zone for crack-free cooling[3]. Tremsin et al. used cold, thermal, and epi-thermal neutron radiography to image europium concentration variations and crystal cracking in situ during growth in a Bridgman furnace, discovering that cracks propagated from clusters of low europium concentration[4,5]. In particular, through real-time visual inspection of Eu-doped BaBrCl in transparent Bridgman and Czochralski furnaces, our group has observed cracking during cooling around 400°C (well below the melting temperature of 886°C). While it is known that the Eu dopant is substitutional on the Ba site, no data on the lattice expansion along the a-, b-, and c-axes of the BaBrCl orthorhombic crystal structure were previously available to allow modeling of thermal and chemical stresses. Similarly, the effect of Eu dopant on the high temperature behavior was unknown. A better understanding of the anisotropic thermal expansion and the strain in BaBrCl at high temperatures and with varying Eu concentrations prompted this study. The results should allow more accurate modeling of thermal and chemical stresses, which should ultimately lead to improved yield during crystal growth.

For the study of BaBrCl, neutron diffraction was selected over X-ray diffraction because it offers better depth of sampling, broader d-spacing spectra, and finer element discrimination. BaBrCl is composed of heavy elements for $\gamma$-ray detection and is thus inherently opaque to X-rays, leading to small volumes probed by X-rays. The Cu-K$\alpha$ X-ray absorption cross sections for BaBrCl and BaBrCl:Eu 5% are 31433 barn and 31833 barn (1 barn = $10^{-28}$ m$^2$), respectively, compared to thermal neutron absorption cross-sections of 13.8 barn and 89.3 barn, respectively[6,7]. This corresponds to absorption lengths of 10 $\mu$m for 8 keV X-rays in both samples, versus 23 mm and 4 mm for thermal neutrons in BaBrCl and BaBrCl:Eu 5%, respectively. In this case, the significantly higher sampling depth of neutrons allows us to increase the sampling volume, neglect any surface effect, and thus provide a more accurate measurement of bulk properties. Neutrons also hold an advantage because the form factor occurring in X-ray diffraction limits the usable d-spacing range over which diffraction peaks can be utilized to determine the crystal structure. Additionally, neutrons provide better sensitivity to the lighter atoms in the sample and less of a difference overall between a group of elements with disparate atomic numbers. In this case, with elements Ba, Br, Cl, and Eu, the Cu-K$\alpha$ X-ray coherent scattering cross section of the least-interacting element, Cl (54.6 barn), is only 5% that of most-interacting element, Eu (1090 barn)[6]. In contrast, for thermal neutrons, the coherent scattering cross section of the least-interacting element, Ba (3.23 barn), is 28% that of the most-interacting element, Cl (11.5 barn)[7]. Thus for this material, neutrons have a smaller range of cross-sections, improving the sensitivity to each element.

Therefore, this study uses high-temperature neutron diffraction

[a] Wake Forest University, Winston-Salem, NC 27109, USA.
[a] Lawrence Berkeley National Laboratory, Berkeley, CA 94720, USA.
[a] University of California at Berkeley, Berkeley, CA 94720, USA.
[b] Los Alamos National Laboratory, Los Alamos, NM 87545, USA

to measure the lattice parameters, atomic positions, and displacements in undoped and 5 mol% Eu-doped BaBrCl for temperatures from 30°C to 800°C. While the crystal structure has been determined before for varying halide ratios, using both X-rays[2,8] and neutrons[9], the effect of high temperature on the structure has not been evaluated previously. By conducting neutron diffraction on powder samples at temperatures up to 800°C (approaching the BaBrCl melting point of 886°C), this study can examine the anisotropic thermal strains which are exacerbated by nonuniform thermal gradients and europium doping during the growth process of bulk single crystals.

## 2 Experiment

### 2.1 Crystal Growth

Undoped BaBrCl and 5% Eu-doped BaBrCl were synthesized following a non-directional solidification technique using 5N (99.999%) pure anhydrous beads of $BaCl_2$, $BaBr_2$, and $EuBr_2$ from Sigma-Aldrich as starting material. Because BaBrCl is hygroscopic, the sample preparation, weighing, and ampoule encapsulation were done in an argon-filled dry box maintained below 0.1 ppm of $O_2$ and $H_2O$. The ampoules were then sealed under dynamic vacuum pumping and placed in a horizontal furnace heated to 920°C to melt the BaBrCl and held at this temperature for 12 hours in order to homogenize the liquefied contents of the quartz ampoule. After solidification (cooled in 48 hours), the samples were transferred back inside the dry box and were ground using a mortar and pestle into a polycrystalline solid for the powder diffraction. Each polycrystalline BaBrCl sample was then placed in a vanadium can with inner diameter 6 mm, sealed with 4 screws and double Ziploc bags to minimize sample degradation before the measurement.

### 2.2 Neutron Diffraction Data Acquisition

High temperature neutron diffraction measurements were obtained using the high-pressure preferred orientation (HIPPO) neutron diffractometer at the Lujan Neutron Scattering Center at Los Alamos National Laboratory[10,11]. The vanadium cans holding the samples were placed in a vacuum furnace in the neutron beam. Just before placing a can in the vacuum furnace setup, the screws were loosened slightly to allow for pressure release of the Ar gas at high temperatures. Neutron time-of-flight data were collected at different temperatures during heating and cooling. Diffraction patterns were collected for the two compounds at temperatures shown in Table 1. Heating and cooling were conducted at the rate of 20°C/min. Taking data points at both increasing and decreasing temperatures allows for examination of any possible hysteresis. To further ensure that preferred crystal orientation did not affect the results, data were collected at each temperature for three sample orientations of 0°, 67°, and 90° rotation about the vertical axis. Neutrons were detected with 39 of the 45 HIPPO detector panels of $^3$He detector tubes arranged on five rings with nominal diffraction angles of $2\theta$ = 39°, 60°, 90°, 120°, and 144°. The remaining detector panels were disabled as they are blocked by the water cooling of the furnace. After confirming that the crystals were oriented randomly, using texture analysis procedures described by ref[12], the data at each detector bank were binned together for all the rotations at each temperature to improve statistics. As demonstrated by ref[13], this procedure would also ensure a uniform polycrystalline representation even if a weak texture is present.

| Temperature [°C] | BaBrCl undoped | BaBrCl: 5% Eu-doped |
|---|---|---|
| 30 | heating | heating |
| 200 | heating | cooling |
| 400 | heating | heating |
| 500 | cooling | – |
| 600 | heating | cooling |
| 700 | cooling | – |
| 800 | heating | heating |

**Table 1** Overview of temperatures at which diffraction data was collected.

### 2.3 Parameter Extraction from Diffraction Data

Neutron diffraction data were analyzed for all five rings simultaneously using the Rietveld method[14] using the General Structure Analysis System (GSAS)[15], automated by scripts through gsaslanguage[16]. The script ensures not only application of identical analysis to each dataset, but also documentation of the refinement steps. A number of parameters were refined to fit the experimental data: 12 background parameters, the lattice parameters, atomic positions (allowing calculation of bond lengths), peak widths, absorption parameters, and anisotropic thermal motion parameters. Additionally, the diffraction constant DIFC, an instrument calibration parameter which takes into account the sample position as well as the geometry of the absorption of the neutron beam in a particular sample, was fit at the first temperature for each sample and held constant across all other temperatures, thus essentially recalibrating the sample position in the instrument. An initial calibration of the DIFC values used lattice parameters previously measured by X-rays. The absorption parameters accounting for each material's absorption of the incident neutrons were similarly fit only for the room temperature measurement and held constant across the other temperatures measured. The crystal structure determined by Hodorowicz et al.[8] was imported from the Inorganic Crystal Structure Database (ICSD)[17]. The downloaded structure had the Br and Cl atom coordinates reversed, which must have been an error in the ICSD data entry since the Hodorowicz paper reported them correctly. To identify this problem, the fractional occupation parameters were allowed to vary for the halide atomic positions in the crystal structure to ensure that the Cl and Br sites were correctly identified. Rietveld fitting using these extra parameters correctly identified the location of the Br and Cl atoms: it placed the Cl at the position (x,y,z) = (0.14, 0.25, 0.43) and Br at the other halide site (x,y,z) = (0.03, 0.25, 0.83) in the orthorhombic structure with a Pnma space group, agreeing with the halide locations found by both previous studies of the BaBrCl structure[2,8]. Having the halides switched in the structure shows up as a missing peak around d-spacing of 6.2 Å. Structural files were visualized using VESTA[18].

After extracting lattice parameters from the Rietveld analysis, we were able to compute temperature-dependent coefficients of

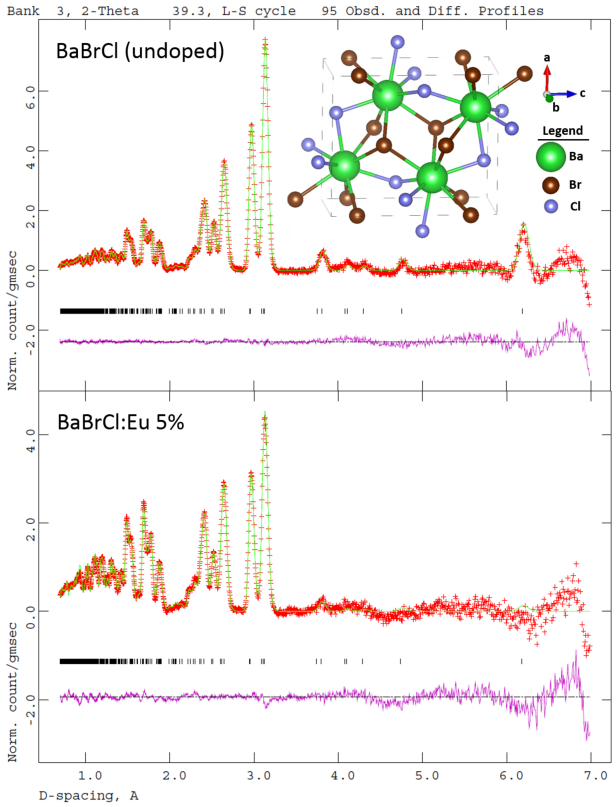


**Fig. 1** Rietveld fits on the data from the 39° detector bank at 30°C for undoped BaBrCl and 5% Eu-doped BaBrCl. (Simultaneously refined diffraction data from the four other detector rings is omitted for space considerations.) This particular detector bank includes a noticable amount of instrument broadening; however, it offers the clearest view of the 6.2 Å peak. The calculated spectrum (green solid line) fits the observed spectrum (red + symbols) well, and the peak markers and difference are displayed below this. The insert shows the unit cell of the BaBrCl material (Eu substitutes at the Ba site). The peak intensities (but not positions) shift due to strong Eu absorption.

| Temperature [°C] | $R_{wp}$ [%] undoped | $R_{wp}$ [%] 5% Eu-doped |
|---|---|---|
| 30 | 0.0077 | 0.0072 |
| 200 | 0.0074 | 0.0067 |
| 400 | 0.0073 | 0.0065 |
| 500 | 0.0074 | – |
| 600 | 0.0072 | 0.0063 |
| 700 | 0.0071 | – |
| 800 | 0.0071 | 0.0061 |

**Table 2** Accuracy of the Rietveld refinement fit to the experimental data

thermal expansion (CTEs) for each lattice parameter and the unit cell volume by using the Thermal Expansion Visualization (TEV) program[19]. Using TEV, second order polynomial fits were applied to the error-weighted lattice parameters vs temperature (all $R^2$ values $> 0.996$). These polynomials and their derivatives are used to generate the second order tensor describing the thermal expansion.

## 3 Results & Discussion

The Rietveld analysis provided good fits to the data (Figure 1), as measured by the weighted pattern R index, $R_{wp}$ (Table 2), and the

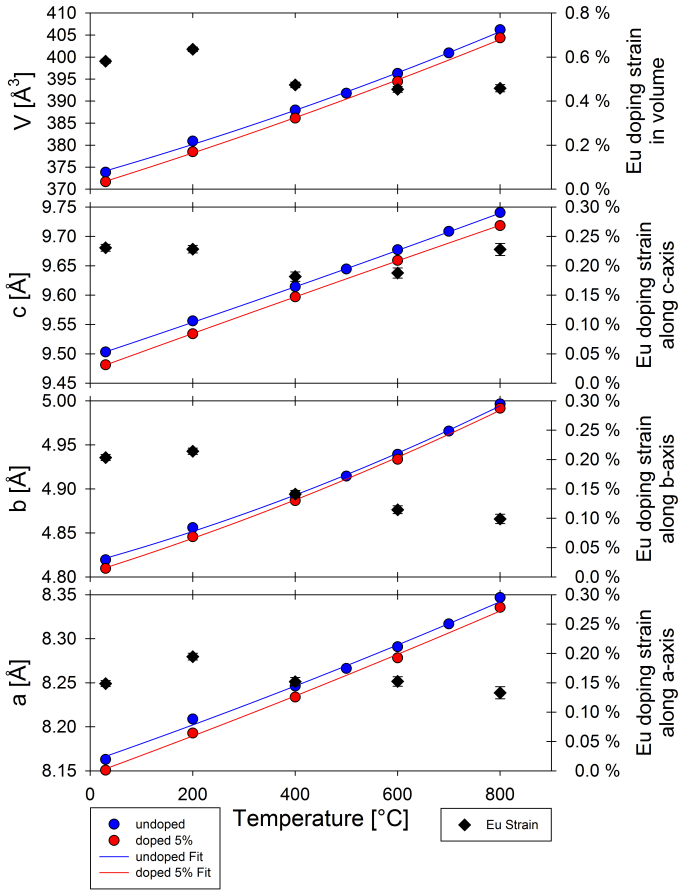


**Fig. 2** On the left axis, the lattice parameters and the unit cell volumes are plotted as a function of temperature for the undoped and 5% Eu-doped BaBrCl crystals. The error bars are smaller than the data markers. On the right axis, the relative strain of contraction induced by the Eu along each crystallographic axis is plotted.

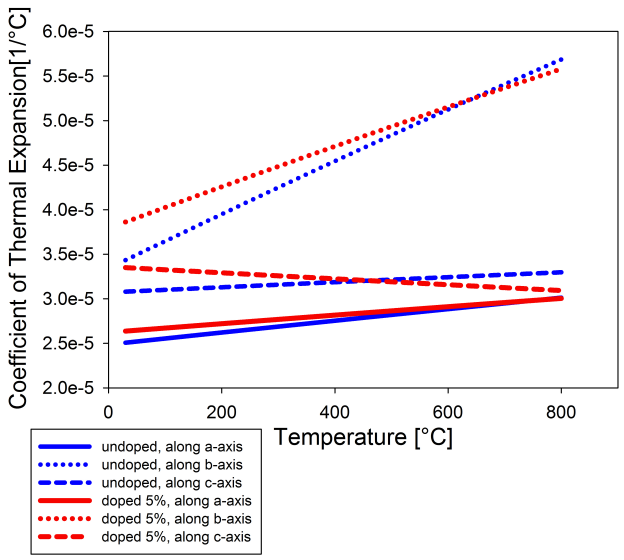


**Fig. 3** CTEs for each crystallographic axis are plotted for the undoped and doped crystals. These curves are calculated from the regressions fit in Figure 2.

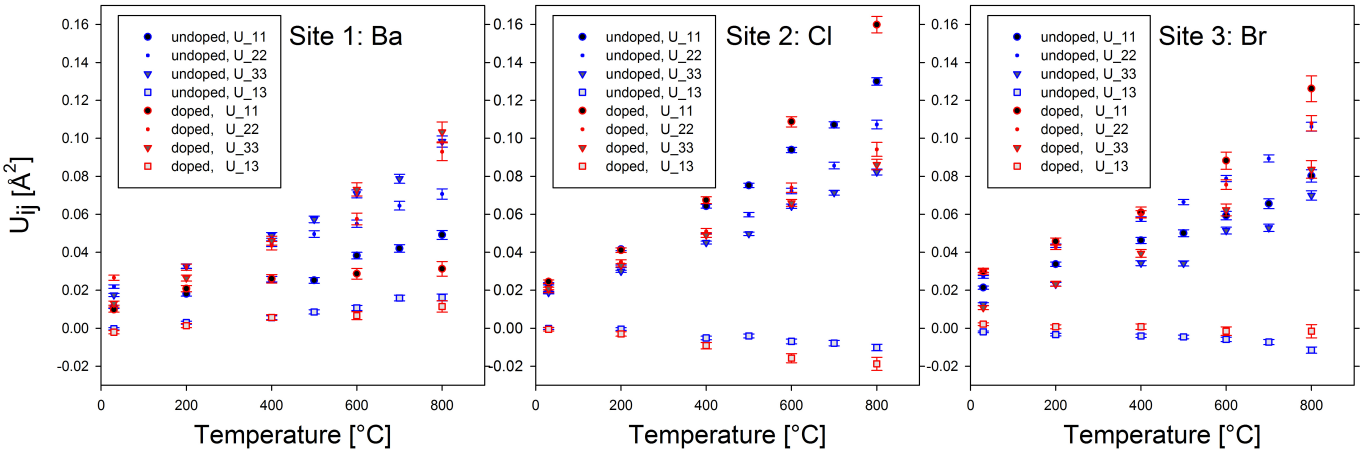


**Fig. 4** Anisotropic thermal motion is plotted along each crystallographic axis. $U_{11}$ corresponds to the vibrational energy along the a-axis; $U_{22}$ for the b-axis; $U_{33}$ for the c-axis. $U_{13}$ is the shear motion.

fit error, $\chi^2$, as well as visual inspection of the difference curves. The diffraction data analysis did not show any indication of preferred orientation in the materials. No other phases were present beyond the expected orthorhombic phase. The quality of the Rietveld fit lends credibility to the crystal properties measured.

Using the tools available in gsaslanguage, diffraction spectra can be simulated based on the crystal structure alone, ignoring any affects from absorption. For the undoped and 5% Eu-doped BaBrCl crystal structures, these simulations predict no significant difference between the two diffraction spectra. However, europium is a strong absorber for thermal neutrons (4500 barn), whereas Ba (1.1 barn), Br (6.9 barn), and Cl (33.5 barn) are all relatively weak absorbers[7]. As seen in Figure 1, this strong neutron absorption does not affect the diffraction peak positions but instead attenuates the peak intensities, with greater attenuation at higher d-spacings, as expected. The absorption parameters taken into account in the Rietveld refinement correct for this absorption so that it does not affect the measurement of other parameters such as the lattice parameters or atomic positions.

Lattice parameters were extracted from the Rietveld analysis (Figure 2). The secondary axis in Figure 2 is used to plot the strain caused by the Eu doping along each lattice parameter: Eu doping strain of contraction along $a_i = (a_{i,undoped} - a_{i,doped})/a_{i,undoped}$. The three orthorhombic lattice parameters in the Eu-doped sample are smaller by 0.15 to 0.25% at room temperature relative to the undoped sample, leading to a volume contraction by 0.6% with 5 mol% Eu doping at room temperature. The relative differences remain approximately constant for all observed temperatures except for the b-axis. Along the b-axis, the difference between doped and undoped material changes from 0.2% at room temperature to 0.1% for temperatures above 400°C, leading to a corresponding volume strain change from 0.6% at room temperature to 0.45% at higher temperatures. In other words, when cooling from 800°C to 200°C, the strain doubles at around 400°C along the b-axis while remaining approximately constant along the other axes.

The TEV software generated the temperature-dependent thermal expansion tensor. Because BaBrCl is an orthorhombic structure, this tensor is a diagonal matrix with each element representing the CTE along that axis of the crystal (Figure 3)[20]. The b-axis is the shortest axis of the unit cell, however it has the highest and fastest growing CTE. The doped sample starts with slightly higher CTEs than the pure material, but the increase of the expansion rate with temperature is smaller in the doped material. For the a- and b-axes, the CTEs at 800°C are the same as for the undoped sample. For the c-axis, the Eu doping resulted in a decrease in thermal expansion rate (not a negative thermal expansion) with temperature.

Figure 4 shows the anisotropic thermal motion for undoped and doped BaBrCl. Along each crystallographic axis, the thermal motion strictly increases with temperature. For the Ba/Eu-site, the thermal motion is greatest along the c-axis, and the Eu doping seems to damp motion along the a-axis, but not along other directions. The Cl ion vibrates about 50% further along the a-axis than along the c-axis, and Eu doping seems to increase that anisotropy. The Br ion vibrates the most along the b-axis in the undoped sample and most along the a-axis in the doped sample.

Bond lengths can be computed from the lattice parameters and atomic positions determined from the Rietveld analysis and are shown in Figure 5 (see Figure 6 for relative changes). In the BaBrCl crystal structure, each Ba has five Br bonds and four Cl bonds. However, there are three crystallographically different bond lengths for Ba-Br bonds and three for Ba-Cl bonds. The Ba-Cl bonds are all shorter and therefore stronger than the Ba-Br bonds. For both Ba-Br and Ba-Cl bonds, two shorter bonds exist (Ba-$Br_I$, Ba-$Br_{II}$ and Ba-$Cl_I$, Ba-$Cl_{II}$) which show a much smaller change with temperature than the third, longer and therefore weaker bond (Ba-$Br_{III}$ and Ba-$Cl_{III}$). All bond lengths increase with temperature, and this increase is mostly linear in the undoped sample but distinctly non-linear in the Ba-Br bonds of the doped sample, with a change in slope observed between the 400°C and 600°C data points. Temperature-induced changes in the bond lengths and lattice parameters can be viewed as thermal strain, $(r(T) - r(T_0))/r(T_0)$, calculated relative to the room temperature bond length, $r(T_0)$ (Figure 6). In both the undoped and doped crystals, the longest Ba-Br and Ba-Cl bonds (Ba-$Br_{III}$ and

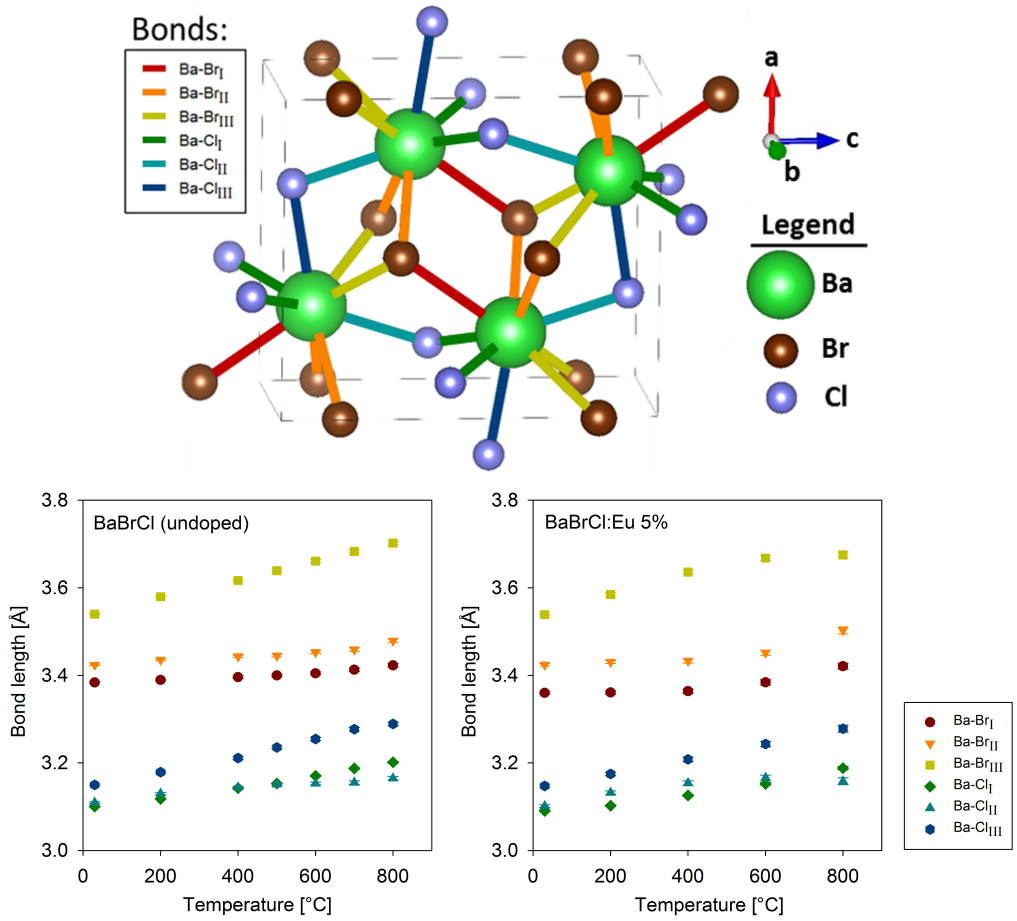


**Fig. 5** Bond lengths for the undoped and doped crystals are plotted versus temperature. The error bars are on the order of the data markers.

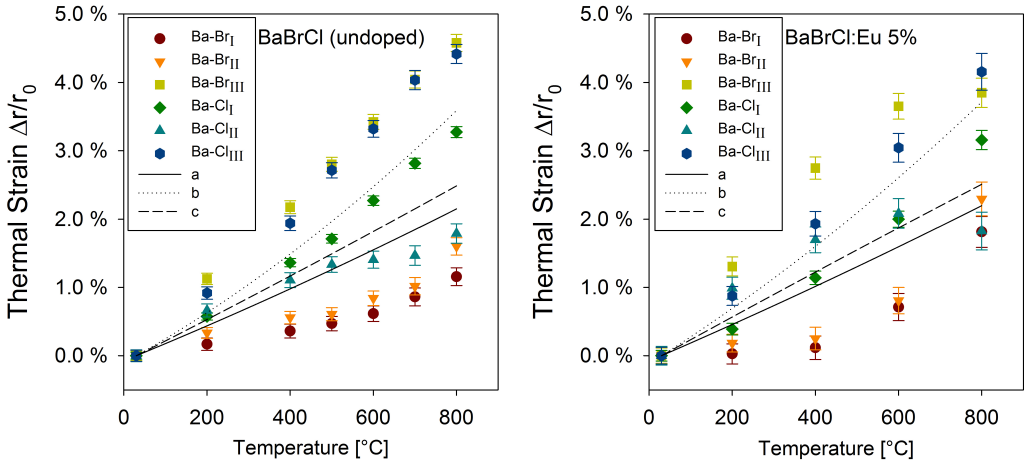


**Fig. 6** Bond lengths and lattice parameters are plotted as thermal strain, with expansion relative to the length at room temperature.

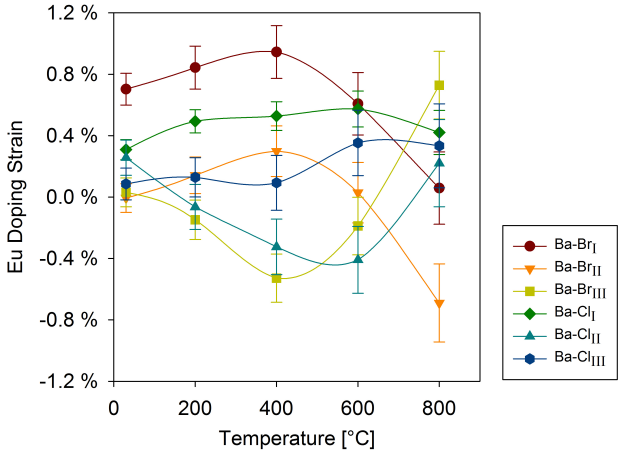


**Fig. 7** Strain from Eu doping for each bond. Negative values indicate contraction of the bond, while positive values indicate expansion due to Eu doping for a given temperature.

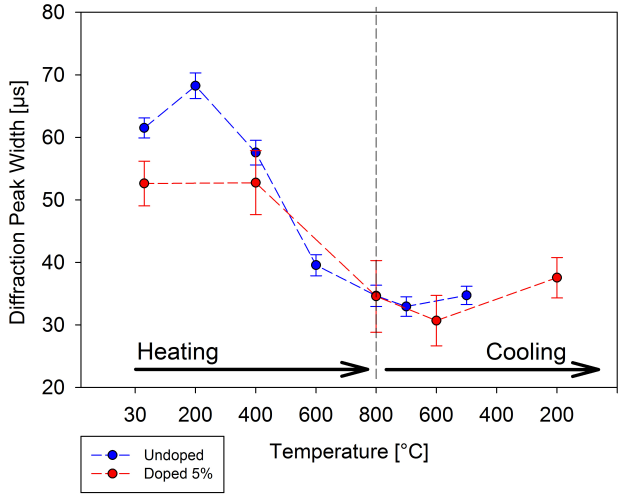


**Fig. 8** In both the undoped and 5% Eu-doped samples, the diffraction peak width demonstrated clear hysteresis, presumably due to an annealing effect. This data was measured by the 144° bank, which provides the highest resolution with the least instrument broadening.

Ba-Cl$_{III}$) have the greatest thermal strain, consistent with them being the weakest bonds. As computed from data shown in Figure 2, the thermal strain along the b-axis (roughly 4% max) is nearly twice as large as along a-axis and c-axis (roughly 2% max). This can be attributed mainly to the Ba-Cl$_{III}$ bond which is directed predominantly along the b-axis (whereas the Ba-Br$_{III}$ bond points approximately along the [111] direction of the crystal, evenly distributing its large thermal expansion across the three axes). Change in the bond lengths due to doping can be viewed in Figure 7 as Eu-induced strain of each bond length, calculated as $(r_{undoped}(T) - r_{doped}(T))/r_{undoped}(T)$. Across temperature, the change in bond lengths due to doping remains under 1%, likely because the Eu and Ba ions both have similar atomic radii and the same 2+ valence state. However, the Eu doping strain in the longer Ba-Br bonds exhibits a greater variation with temperature than in the shorter Ba-Cl bonds. Additionally, the three Ba-Br bonds all exhibit a reversal from expansion to contraction and vice-versa around 400°C.

With the exception of the peak width parameters, for all parameters discussed above, the parameter values for heating and cooling overlaid along the same trendline. For the diffraction peak width, a non-reversible decrease was observed during heating for both compounds (Figure 8), consistent with annealing, i.e. removal of defects in the crystal lattice.

## 4 Conclusions

For the first time, the lattice parameters and atomic positions of undoped and 5% Eu-doped BaBrCl were measured at high temperatures approaching the melting point using neutron diffraction. Analysis of the Rietveld refinement data produced measurements of the temperature-dependent thermal expansion tensor, anisotropic thermal motion for each atom, and both thermal and dopant-induced strain along each bond and axis. We have measured greater thermal expansion and thermal strain along the b-axis than along the a- and c-axes by almost a factor of two. We have also observed that the BaBrCl host structure shows a smaller volume strain due to the incorporation of Eu atoms at temperatures above 400°C compared to below 400°C, with the majority of that change occurring along the b-axis and Ba-Br bonds. This change in ability to accommodate dopant atoms around 400°C may explain the observation of cracks occurring in that temperature range during cooling of single crystals during growth. This chemical strain adds to thermal strain caused by temperature inhomogeneity in the crystal, suggesting that slower cooling rates should be employed in that temperature range to minimize thermal gradients. Since the b-axis shows such a significant change in thermal expansion, orienting the crystal with that axis along the lowest thermal gradient may further reduce the risk of fracture. Detailed thermo-mechanical modeling of single crystals, utilizing the data obtained in this study from powder materials, will guide our conclusions to optimize the growth process and ultimately increase the growth yield of scintillator crystals.

## 5 Acknowledgements

This work has benefited from the use of the Lujan Neutron Scattering Center at LANL, which is operated by Los Alamos National Security LLC under DOE contract DEAC5206NA25396. We acknowledge DOE/NNSA DNN R&D funding of project LB15-V-GammaDetMater-PD3Jf and Lawrence Berkeley National Laboratory for subcontract support of Wake Forest University under the NNSA Multi-Laboratory Collaboration. We also wish to thank Shyam Dwaraknath from Lawrence Berkeley National Laboratory and Sergii Gridin from Wake Forest University for helpful discussion.

## References

## Notes and references

1 Bourret-Courchesne, E. D., Bizarri, G. A., Borade, R., Gundiah, G., Samulon, E. C., Yan, Z. & Derenzo, S. E. (2012). *J. Cryst. Growth* **352**, 78–83.

2 Gundiah, G., Yan, Z., Bizarri, G., Derenzo, S. E. & Bourret-

Courchesne, E. D. (2013). *J. Lumin.* **138**, 143-149.

3 Yan, Z., Shalapska, T. & Bourret, E. D. (2016). *J. Cryst. Growth* **435**, 42-45.

4 Tremsin, A. S., Makowska, M. G., Perrodin, D., Shalapska, T., Khodyuk, I. V., Trtik, P., Boillat, P., Vogel, S. C., Losko, A. S., Strobl, M., Kuhn, L. T., Bizarri, G. A. & Bourret-Courchesne, E. D. (2016). *J. Appl. Cryst.* **49**, 743–755.

5 Tremsin, A. S., Perrodin, D., Losko, A. S., Vogel, S. C., Bourke, M. A. M., Bizarri, G. A. & Bourret, E. D. (2017). *Sci. Rep.* **7**, 46275.

6 Berger, M. J., Hubbell, J. H., Seltzer, S. M., Chang, J., Coursey, J. S., Sukumar, R., Zucker, D. S. & Olsen, K. (2010). *XCOM: Photon Cross Section Database*, https://www.nist.gov/pml/xcom-photon-cross-sections-database. National Institute of Standards and Technology, Gaithersburg, MD, USA.

7 Sears, V. F. (1992). *Neutron News* **3**(3), 26–37.

8 Hodorowicz, S. A., Hodorowicz, E. K. & Elck, H. A. (1983). *J. Solid State Chem.* **48**, 351–356.

9 Eick, H. A. & Prince, E. (1986). *Acta Cryst. C***42**, 915–917.

10 Wenk, H.-R., Lutterotti, L. & Vogel, S. (2003). *Nucl. Instrum. Methods Phys. Res. A* **515**, 575–588.

11 Vogel, S. C., Hartig, C., Lutterotti, L., Von Dreele, R. B., Wenk, H.-R. & Williams, D. J. (2004). *Powder Diffr.* **19**, 65–68.

12 Wenk, H.-R., Lutterotti, L. & Vogel, S. C. (2010). *Powder Diffr.* **25**, 283–296.

13 Bruno, G. & Vogel, S. C. (2017). *J. Appl. Cryst.* **50**, 749–762.

14 Rietveld, H. M. (1969). *J. Appl. Cryst.* **2**, 65–71.

15 Larson, A. C. & Von Dreele, R. B. (2004). *GSAS.* Report LAUR 86-748. Los Alamos National Laboratory, New Mexico, USA

16 Vogel, S. C. (2011). *J. Appl. Cryst.* **44**, 873–877.

17 Bergerhoff, G., Hundt, R., Sievers, R. & Brown, I. D. (1983). *J. Chem. Inf. Model.* **23**, 66–69.

18 Momma, K. & Izumi, F. (2011). *J. Appl. Cryst.* **44**, 1272–1276.

19 Langreiter, T. & Kahlenberg, V. (2015). *Crystals* **5**, 143–153.

20 Nye, J. F. (1985). *Physical Properties of Crystals: Their Representation by Tensors and Matrices*. Oxford: Clarendon Press.